International Journal of Basic and Applied Sciences, 14 (8) (2025) 106-120

International Journal of Basic and Applied Sciences

Website: www.sciencepubco.com/index.php/IJBAS
https://doi.org/10.14419/9pjcye33
Research paper

Fractional-Order Modeling and Neural Network Simulation of NK Cell-Oncolytic Virus Interactions

M. Sharmila *, S. Indrakala

Department of Mathematics, Kunthavai Naacchiyaar Government Arts College for Women(Autonomous),
("Affiliated to Bharathidasan University" Tiruchirappalli, 620024), Thanjavur - 613007,
Tamil Nadu, India
**Corresponding author E-mail: schitrarmohan@gmail.com*

Received: October 16, 2025, Accepted: November 22, 2025, Published: December 4, 2025

Abstract

Oncolytic virotherapy (OV) uses viruses to selectively destroy cancer cells, but the role of natural killer (NK) cells in this process remains unclear. This study develops a discrete fractional-order model to examine NK cell activity and identify activation conditions. Existence of the model solution is established via fixed-point theorems, and the basic reproduction number (R_0) is derived using the next-generation matrix method with sensitivity analysis to determine key parameters. Stability of equilibria is analyzed, and numerical simulations reveal how NK cell activation affects interactions among cancer cells, infected cells, and viruses. Additionally, an artificial neural network (ANN) trained with the Levenberg-Marquardt algorithm efficiently approximates the model's dynamics, showing high accuracy (low MSE) and providing a rapid, reliable tool for predicting complex biological behaviors.

Keywords: *Oncolytic Virotherapy; Mathematical Modeling; Discrete Fractional-Order Model; Existence Theory; Stability Analysis.*

1. Introduction

Oncolytic virotherapy (OV) employs engineered lytic viruses that selectively replicate in cancer cells, destroying them while sparing healthy tissue. This tumor-specific targeting offers advantages over conventional treatments like chemotherapy and radiation. Several engineered viruses-such as adenovirus, herpesvirus, and measles virus-are in clinical trials, with T-VEC (IMLYGIC®) being the first FDA-approved OV for melanoma. Promising clinical results have also been reported for glioblastoma using recombinant polio-rhinovirus therapy [9], [16], [19], [20], [25], [27], [28], [35], [44]. Tumor destruction in OV occurs through direct viral lysis and immune-mediated mechanisms involving NK and T cells. While NK cell activation can enhance viral therapy efficacy, as shown in ovarian and hepatocellular cancer studies, excessive immune responses may prematurely clear infected cells, limiting viral replication. Balancing antiviral immunity and viral propagation is therefore crucial for successful virotherapy [8], [12], [21], [39]. Mathematical modeling continuous or discrete provides insight into these interactions. Prior models have examined immune responses, viral burst size, and NK cell recruitment, showing their roles in tumor suppression and equilibrium dynamics. Building on these studies, Kim et al. developed a model analyzing how NK cells affect OV efficacy, assuming logistic tumor growth, virus specificity for cancer cells, one-to-one infection dynamics, and NK targeting of both uninfected and infected tumor cells [3], [26], [40].

$$\begin{cases} u'(t) = \Xi u(t)\left(1-\frac{u(t)}{C}\right) - \varpi_1 u(t)p(t) - \chi u(t)q(t), \\ v'(t) = \varpi_1 u(t)p(t) - \psi v(t)q(t) - \Delta_1 v(t), \\ p'(t) = a_p \Delta_1 v(t) - \varpi_1 u(t)p(t) - \Delta_2 p(t), \\ q'(t) = \Xi_q v(t)q(t) - \Delta_3 q(t). \end{cases} \tag{1}$$

The variables u, v, p, q denote cancerous, infected, free virus, and NK cell populations, respectively. Cancer cells follow logistic growth modeled by $\Xi u\left(1-\frac{u}{C}\right)$, where Ξ denotes how quickly the population of cancer cell grows, and C stands for the tumor's carrying capacity. Viral infection of cancer cells occurs at a rate $\varpi_1 up$, with ϖ_1 representing infectivity. NK cell-mediated killing rates of cancer and infected cells are denoted by χ and ψ, respectively. Infected cells undergo lysis at rate Δ_1, releasing a_p virus particles per cell (viral burst size), where a_p denotes the viral burst size, while free virus is cleared at rate Δ_2. Infected cells stimulate NK cell production at rate $\Xi_{\gtrsim}$, and NK cells are cleared at rate Δ_3.
Time dependence is suppressed in Equation 1 for clarity. Equation 1 becomes:

$$\begin{cases} \tilde{u}'(\varsigma) = \frac{\Xi}{\Delta_1}\tilde{u}(\varsigma)\big(1-\tilde{u}(\varsigma)\big) - \frac{\varpi_1 C}{\Delta_1}\tilde{u}(\varsigma)\tilde{p}(\varsigma) - \frac{\chi C}{\Delta_1}\tilde{u}(\varsigma)\tilde{q}(\varsigma) \\ \tilde{v}'(\varsigma) = \frac{\varpi_1 C}{\Delta_1}\tilde{u}(\varsigma)\tilde{p}(\varsigma) - \frac{\psi C}{\Delta_1}\tilde{v}(\varsigma)\tilde{q}(\varsigma) - \tilde{v}(\varsigma) \\ \tilde{p}'(\varsigma) = a_p\tilde{v}(\varsigma) - \frac{\varpi_1 C}{\Delta_1}\tilde{u}(\varsigma)\tilde{p}(\varsigma) - \frac{\Delta_2}{\Delta_1}\tilde{p}(\varsigma) \\ \tilde{q}'(\varsigma) = \frac{\Xi_q C}{\Delta_1}\tilde{v}(\varsigma)\tilde{q}(\varsigma) - \frac{\Delta_3}{\Delta_1}\tilde{q}(\varsigma) \end{cases} \quad (2)$$

By introducing the scaled parameters:

$$k_1 = \frac{\Xi}{\Delta_1}, b_u = \frac{\varpi_1 C}{\Delta_1}, c_1 = \frac{\chi C}{\Delta_1}, c_2 = \frac{\psi C}{\Delta_1}$$
$$k_2 = \frac{\Xi_{\geq} C}{\Delta_1}, \Delta_p = \frac{\Delta_2}{\Delta_1}, \Delta_q = \frac{\Delta_3}{\Delta_1}$$

The system is rescaled for simplicity. Let

$$\tilde{u} = u, \tilde{v} = v, \tilde{p} = p, \tilde{q} = q, \varsigma = t.$$

Then, system 2 becomes:

$$\begin{cases} u'(t) = k_1 u(t)\big(1-u(t)\big) - b_u u(t)p(t) - c_1 u(t)q(t) \\ v'(t) = b_u u(t)p(t) - c_2 v(t)q(t) - v(t) \\ p'(t) = a_p v(t) - b_u u(t)p(t) - \Delta_p p(t) \\ q'(t) = k_2 v(t)q(t) - \Delta_q q(t) \end{cases} \quad (3)$$

Fractional calculus (FC), originating from the early foundations of classical calculus [20], has developed into a powerful mathematical framework for describing complex real-world systems—especially those characterized by memory and hereditary effects that traditional calculus cannot adequately represent. Incorporating short- and long-term memory into mathematical models helps reveal fundamental mechanisms driving disease transmission, which may otherwise remain undetected if memory effects are neglected. For example, memory plays a crucial role in immune system behavior, and recognizing this influence supports the development of more effective disease control strategies [1], [2], [4], [5-15].

Beyond biological applications, FC has proven highly versatile across numerous scientific and engineering disciplines. Its uses span disease modeling [18], [21], blood flow analysis [22], bioengineering [23], and experimental data fitting [24], as well as fluid mechanics [25], viscoelasticity [26], electrochemistry [27], electrodynamics in complex media [28], thermodynamics [29], and aerodynamics [30]. In engineering, FC contributes to advancements in control theory [31], electrical circuits [32], capacitor modeling [33], robotics [34], and optical fiber systems [35]. Owing to its flexibility and modeling advantages, FC continues to shape emerging research areas in physics, polymer technologies [36], and other advanced applications [37].

The literature provides a wide range of fractional-order operator formulations, each offering distinct benefits and limitations [38]. Among them, the discrete fractional-order difference operator serves as a key generalization of classical difference equations. Since empirical data are frequently recorded at discrete time intervals, fractional difference operators are particularly effective for representing such systems, producing results naturally aligned with data structure. Their applicability extends across multiple fields, including electrical engineering [38], [39], neural networks [40], game theory [40], [41], epidemiology [42], image processing [43].The formal definitions, related remarks, and supporting lemmas for the fractional difference operator are presented below.

Definition 1: *[29] The fractional difference of order τ in the Caputo sense, applied to a function $g(t)$, is defined as:*

$$^{\mathcal{C}}\eta_a^{\tau} g(t) = \eta_a^{-(m-\tau)}\eta^m g(t) = \frac{1}{\Gamma(m-\tau)}\sum_{s=a}^{t-(m-\tau)} (t-s-1)^{m-\tau-1}\eta^m g(s),$$

Where $t \in \mathbb{N}_{a+m-\tau}, m = \lceil\tau\rceil + 1$ and $\tau > 0$ with $\tau \notin \mathbb{N}$. The corresponding expressions for the falling factorial $(t-s-1)^{(m-\tau-1)}$ and the integer-order difference operator of order m, denoted by $\eta^m g(s)$, are provided below:

$$(t-s-1)^{(m-\tau-1)} = \frac{\Gamma(t-s)}{\Gamma(t-s-m+\tau+1)}$$

And

$$\eta^m g(t) = \eta\big(\eta^{m-1} g(t)\big) = \sum_{n=0}^{m} \binom{m}{n}(-1)^{m-n} f(t+n), t \in \mathbb{N}_a$$

Definition 2: *[29] Consider a function $g(t)$ that maps discrete time points in $\mathbb{N}_a$ to real numbers. The fractional sum of order τ associated with g is given by:*

$$\eta_a^{-\tau} g(t) = \frac{1}{\Gamma(\tau)}\sum_{s=a}^{t-\tau} (t-s-1)^{\tau-1} g(s)$$

Where $\tau > 0, t$ belongs to the time scale $\mathbb{N}_{a+\tau} = a+\tau, a+\tau+1, \ldots$, and $a \in \mathbb{R}$.

Existence theory, grounded in fixed-point theorems, provides a key framework for analyzing nonlinear problems across mathematics and engineering. These theorems simplify complex functional equations by reformulating them as fixed-point problems, aiding studies in optimization, equilibrium analysis, and differential equations. [4]. Building on this foundation, the present study explores the existence and dynamics of an oncolytic virotherapy (OV) model using the discrete Caputo fractional difference operator. Although OV is a continuous biological process, clinical and experimental data are typically recorded at discrete intervals. The discrete fractional framework effectively

captures memory effects while fitting this data structure. It also facilitates numerical simulations and ANN-based learning, offering both analytical precision and computational efficiency. The resulting hybrid model supports accurate, real-time prediction of complex biological dynamics 3 is expressed as follows:

$$\begin{cases} {}^{\mathcal{C}}\eta^{\tau}u = k_1^{\tau}u(t+\tau-1)(1-u(t+\tau-1)) - a_u^{\tau}u(t+\tau-1)p(t+\tau-1) \\ \quad -c_1^{\tau}u(t+\tau-1)q(t+\tau-1), \\ {}^{\mathcal{C}}\eta^{\tau}v = a_u^{\tau}u(t+\tau-1)p(t+\tau-1) - c_2^{\tau}v(t+\tau-1)q(t+\tau-1) - v(t+\tau-1), \\ {}^{\mathcal{C}}\eta^{\tau}p = a_p^{\tau}v(t+\tau-1) - b_u^{\tau}u(t+\tau-1)p(t+\tau-1) - \Delta_p^{\tau}p(t+\tau-1), \\ {}^{\mathcal{C}}\eta^{\tau}q = k_2^{\tau}v(t+\tau-1)q(t+\tau-1) - \Delta_q^{\tau}q(t+\tau-1). \end{cases}$$

The mathematical formulation of model 4 leads to the following system of four equivalent equations:

$$\begin{cases} u(t) = u(0) + \frac{1}{\Gamma(\tau)}\sum_{s=1-\tau}^{t-\tau}(t-s-1)^{\tau-1}\big(k_1^{\tau}u(s+\tau-1)\big(1-u(s+\tau-1)\big) - b_u^{\tau}u(s+\tau-1) \\ \quad \times p(s+\tau-1) - c_1^{\tau}u(s+\tau-1)q(s+\tau-1)\big) \\ v(t) = y(0) + \frac{1}{\Gamma(\tau)}\sum_{s=1-\tau}^{t-\tau}(t-s-1)^{\tau-1}(b_u^{\tau}u(s+\tau-1)p(s+\tau-1) - c_2^{\tau}v(s+\tau-1) \\ \quad \times q(s+\tau-1) - v(s+\tau-1)\big) \\ p(t) = p(0) + \frac{1}{\Gamma(\tau)}\sum_{s=1-\tau}^{t-\tau}(t-s-1)^{\tau-1}\big(a_p^{\tau}v(s+\tau-1) - a_u^{\tau}u(s+\tau-1)p(s+\tau-1) \\ \quad -\Delta_p^{\tau}p(s+\tau-1)\big) \\ q(t) = q(0) + \frac{1}{\Gamma(\tau)}\sum_{s=1-\tau}^{t-\tau}\big(t-s-1)^{\tau-1}\big(k_2^{\tau}v(s+\tau-1)q(s+\tau-1) - \Delta_q^{\tau}q(s+\tau-1)\big) \end{cases} \quad (5)$$

The paper unfolds through several thematic sections. Section 2 is devoted to developing the existence theory for solutions to themodel 4. In Section 3, the model 4 undergoes foundational analysis, covering aspects such as positivity, equilibrium states, the basic reproduction number ($\mathbb{R}_0$), and both sensitivity and scenario analyses. Section 4 showcases numerical simulations alongside ANN results, followed by interpretive discussion. The study concludes in Section 5, which outlines the principal findings and closing perspectives.

2. Existence Theory

This section develops the theoretical framework to demonstrate the existence of solutions to the proposed model 4.
Let each equation in model (5) be associated with a corresponding function as follows:

$$\begin{cases} h_1(t+\tau-1,u,v,p,q) = k_1^{\tau}u(t+\tau-1)(1-u(t+\tau-1)) - b_u^{\tau}u(t+\tau-1)p(t+\tau-1) \\ \quad -c_1^{\tau}u(t+\tau-1)q(t+\tau-1) \\ h_2(t+\tau-1,u,v,p,q) = b_u^{\tau}u(s+\tau-1)p(s+\tau-1) - c_2^{\tau}v(s+\tau-1)q(s+\tau-1) \\ \quad -v(s+\tau-1) \\ h_3(t+\tau-1,u,v,p,q) = a_p^{\tau}v(s+\tau-1) - a_u^{\tau}u(s+\tau-1)p(s+\tau-1) - \Delta_p^{\tau}p(s+\tau-1) \\ h_4(t+\tau-1,u,v,p,q) = k_2^{\tau}v(s+\tau-1)q(s+\tau-1) - \Delta_q^{\tau}q(s+\tau-1) \end{cases} \quad (6)$$

This leads to the following representation of system (5).

$$g(t) = g(0) + \frac{1}{\Gamma(\tau)}\sum_{s=0}^{t-\tau}(t-s-1)^{\tau-1}(\Phi(s+\tau-1,g(s+\tau-1)) \quad (7)$$

Where

$$\mathbf{g(t)} = \begin{cases}\mathbf{u(t)}\\ \mathbf{v(t)}\\ \mathbf{p(t)}\\ \mathbf{q(t)}\end{cases}, \mathbf{f(0)} = \begin{cases}\mathbf{u_0}\\ \mathbf{v_0}\\ \mathbf{p_0}\\ \mathbf{q_0}\end{cases}, \mathbf{\Phi\big(t+\tau-1, g(t+\tau-1)\big)} = \begin{cases}\mathbf{g_1(t+\tau-1,u,v,p,q)}\\ \mathbf{g_2(t+\tau-1,u,v,p,q)}\\ \mathbf{g_3(t+\tau-1,u,v,p,q)}\\ \mathbf{g_4(t+\tau-1,u,v,p,q)}\end{cases}$$

3. Basic Analysis of The Model

This section investigates the qualitative behavior of the model by establishing the non-negativity and boundedness of solutions, determining equilibrium points alongside their stability conditions, deriving the basic reproduction number ($\mathbb{R}_0$), and exploring its sensitivity and outcomes across different hypothetical scenarios.

3.1. Non-negativity and boundedness of solutions

For biological relevance, the solutions of system 4 must remain non-negative over time. Furthermore, due to constraints such as limited resources, these solutions should not grow unbounded. The theorem below confirms that all state variables of system 4 are both positive and bounded throughout the evolution of the system.

3.2. Equilibrium points

Setting the right-hand sides of system 4 to zero yields the equilibrium points of the discrete fractional-order model. Take $X = (u, v, p, q)^T$, and define the nonlinear vector function:

$$G(X) = \left(k_1^\tau u(1-u) - b_u^\tau up - c_1^\tau uq \gtrsim, b_u^\tau up - c_2^\tau vq - v, a_p^\tau v - b_u^\tau up - \Delta_p^\tau p, k_2^\tau vq - \Delta_q^\tau q\right)^T \tag{8}$$

The model takes the form of the following discrete fractional-order system:

$$^{\mathcal{C}}\eta^\tau X(t) = G(X(t+\tau-1)), \tag{9}$$

Where $^{\mathcal{C}}\eta^\tau$ denotes the Caputo fractional difference operator. The equilibrium points correspond to constant solutions for which:

$$^{\mathcal{C}}\eta^\tau X(t) = 0 \text{ for all } t, \tag{10}$$

Which leads to the algebraic system $G(X) = 0$, i.e.,

$$\begin{cases} k_1^\tau u(1-u) - b_u^\tau up - c_1^\tau uq = 0, \\ b_u^\tau up - c_2^\tau vq - v = 0, \\ a_p^\tau v - b_u^\tau up - \Delta_p^\tau p = 0, \\ k_2^\tau vq - \Delta_q^\tau q = 0. \end{cases} \tag{11}$$

Following the procedure outlined in [25], the system admits the following equilibrium points:

$E_0(0,0,0,0), E_1(1,0,0,0)$

$$E_2\left(\frac{\Delta_p^\tau}{b_u^\tau(a_p^\tau-1)}, \frac{k_1^\tau\Delta_p^\tau}{b_u^\tau(a_p^\tau-1)}\left(1-\frac{\Delta_p^\tau}{b_u^\tau(a_p^\tau-1)}\right), \frac{k_1^\tau}{b_u^\tau}\left(1-\frac{\Delta_p^\tau}{b_u^\tau(a_p^\tau-1)}\right), 0\right),$$

$E_3(u_+^*, v^*, p_-^*, q_+^*)$

And

$E_4(u_-^*, v^*, p_+^*, q_-^*)$

Where the subscript + or - corresponds to taking the positive (or negative) sign in front of η in the explicit expressions for u^*, p^*, q^* and

$$\eta = \sqrt{k_2^\tau\Delta_q^{2\tau}\left[k_2^\tau\left(c_1^\tau b_u^\tau(a_p^\tau-1) - c_2^\tau k_1^\tau(b_u^\tau+\Delta_p^\tau)\right)^2 - 4c_2^\tau k_1^\tau b_u^\tau a_p^\tau(c_2^\tau b_u^\tau\Delta_q^\tau - c_1^\tau k_2^\tau\Delta_p^\tau)\right]}$$

$$u^* = \frac{k_2^\tau\Delta_q^\tau\left(c_2^\tau k_1^\tau(b_u^\tau-\Delta_p^\tau) - c_1^\tau b_u^\tau(a_p^\tau-1)\right)\pm\eta}{2c_2^\tau k_1^\tau k_2^\tau b_u^\tau\Delta_q^\tau}$$

$$v^* = \frac{\Delta_q^\tau}{k_2^\tau a}$$

$$p^* = \frac{k_2^\tau\Delta_q^\tau\left(c_2^\tau k_1^\tau(b_u^\tau+\Delta_p^\tau) - c_1^\tau b_u^\tau(a_p^\tau-1)\right)\pm\eta}{2(c_2^\tau b_u^\tau\Delta_q^\tau - c_1^\tau k_2^\tau\Delta_p^\tau)k_2^\tau b_u^\tau}$$

$$q^* = \frac{k_2^\tau b_u^\tau\Delta_p^\tau\Delta_q^\tau(-c_1^\tau(a_p^\tau-1) - c_2^\tau k_1^\tau) + 2c_2^\tau b_u^{2\tau}(a_p^\tau-1)\Delta_q^{2\tau} - c_2^\tau k_1^\tau k_2^\tau\Delta_p^{2\tau}\Delta_q^\tau \pm \Delta_p^\tau\eta}{2(c_2^\tau b_u^\tau\Delta_q^\tau - c_1^\tau k_2^\tau\Delta_p^\tau)c_2^\tau b_u^\tau\Delta_z^\tau}$$

It is important to emphasize that because all model parameters are positive, the expressions for u_-^* and p_+^* evaluate to negative values. Since the positively invariant domain D represents biologically meaningful states—where all population variables must remain non-negative—these negative coordinates violate the domain constraints. Consequently, the equilibrium point $E_4(u_-^*, v^*, p_+^*, q_-^*)$ lies outside the admissible region D and therefore cannot be treated as a biologically or mathematically valid equilibrium of the system.

3.3. Basic reproduction number

This subsection calculates the basic reproduction number ($\mathbb{R}_0$) for the model 4 using the Next Generation Matrix method [17]. Consider the vector $\Theta = (v, u, p)$, which allows the first three equations of system 4 to be expressed in the form $\Theta' = A(\Theta) - B(\Theta)$, where

$$A(\Theta) = \begin{pmatrix} b_u^\tau up \\ 0 \\ 0 \end{pmatrix}, B(\Theta) = \begin{pmatrix} c_2^\tau vq + v \\ -k_1^\tau u(1-u) + b_u^\tau up + c_1^\tau uq \\ -a_p^\tau v + b_u^\tau up + \Delta_p^\tau p \end{pmatrix}.$$

The Jacobian matrices of A and B evaluated at the equilibrium point E_1 are given by:

$$J(A(E_1)) = \begin{pmatrix} 0 & 0 & b_u^\tau \\ 0 & 0 & 0 \\ 0 & 0 & 0 \end{pmatrix}, J(B(E_1)) = \begin{pmatrix} 1 & 0 & 0 \\ 0 & k_1^\tau & b_u^\tau \\ -a_p^\tau & 0 & b_u^\tau + \Delta_p^\tau \end{pmatrix}$$

The basic reproduction number is determined as $\mathbb{R}_0 = \varrho(AB^{-1})$, leading to:

$$\mathbb{R}_0 = \frac{b_u^\tau a_p^\tau}{b_u^\tau + \Delta_p^\tau}. \tag{12}$$

Therefore, the expression in equation 12 represents the basic reproduction number ($\mathbb{R}_0$) associated with the system 4.

3.4. Sensitivity analysis

Conducting a detailed sensitivity analysis of $\mathbb{R}_0$ is essential to evaluate the impact of individual model parameters on the tumor-immune interaction dynamics. To quantify how $\mathbb{R}_0$ responds to variations in a parameter ($\cdot$), the corresponding sensitivity index is defined as:

$$\Sigma_{(\cdot)} = \frac{(\cdot)}{\mathbb{R}_0} \times \frac{\partial \mathbb{R}_0}{\partial (\cdot)} \tag{13}$$

By evaluating the sensitivity index formula with respect to each parameter, the following expressions are obtained:

$$\Sigma_{b_u} = \frac{\tau \cdot \Delta_p^\tau}{b_u^\tau + \Delta_p^\tau} \tag{14}$$

$$\Sigma_{a_p} = \tau. \tag{15}$$

$$\Sigma_{\Delta_p} = -\frac{\tau \cdot \Delta_p^\tau}{b_u^\tau + \Delta_p^\tau}. \tag{16}$$

Substituting $b_u = 0.1$ and $\Delta_p = 0.2$ into 12, Table 1 reports the resulting sensitivity indices, showing the extent and nature of each parameter's influence on $\mathbb{R}_0$ across different fractional orders.
The sensitivity values are presented in Figure 3.4. As τ increases from 0.7 to 1.0, the sensitivity indices of b_u and a_p also increase, indicating that these parameters exert a stronger positive influence.

Table 1: Sensitivity Indices of The $\mathbb{R}_{\psi}$ Against the Parameters.

τ	Σ_{b_u}	Σ_{a_p}	Σ_{Δ_p}
0.7	0.43328	0.70	-0.43328
0.8	0.50815	0.80	-0.50815
0.9	0.58598	0.90	-0.58598
1.0	0.66667	1.00	-0.66667

on $\mathbb{R}_0$ at higher fractional orders. Specifically, the sensitivity of b_u increases from 0.43328 to 0.66667 , and for a_p, it increases linearly from 0.70 to 1.00 . This suggests that small changes in b_u and a_p can lead to more substantial increases in $\mathbb{R}_0$ as the system becomes less fractional and approaches classical dynamics. On the other hand, the sensitivity index for Δ_p becomes more negative (from -0.43328 to -0.66667), indicating a stronger suppressive effect on $\mathbb{R}_0$ with increasing τ. Among all, a_p is the most influential parameter in increasing $\mathbb{R}_0$, while Δ_p is the most effective in decreasing it.

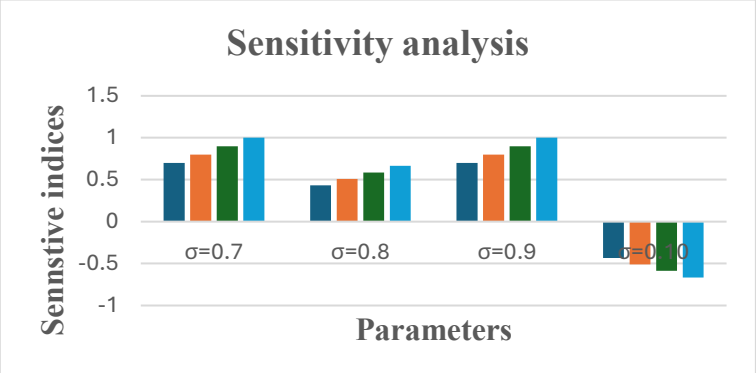

Fig. 1: Sensitivity Analysis Plot Illustrating the Impact of Each Parameter on $\mathbb{R}_0$.

3.5. Scenario analysis

While individual sensitivity analysis of $\mathbb{R}_0$ is informative, examining parameter pairs provides a deeper understanding of system dynamics by capturing synergistic and nonlinear interactions. As illustrated in Figure 3.4, the parameter a_p, which characterizes the viral burst generated during infected cell lysis, emerges as the most influential factor when no external virus is introduced.
Figure 3.5 illustrates the contour plots of $\mathbb{R}_0$ as a function of parameters b_u and Δ_p across different fractional orders. It is evident that $\mathbb{R}_0$ increases with larger values of b_u and decreases with higher Δ_p. As the fractional order τ increases from 0.7 to 1.0, the gradient of $\mathbb{R}_0$ becomes steeper, indicating heightened sensitivity to parameter changes. Figure 3 presents $\mathbb{R}_0$ with respect to a_p and b_u, showing that both parameters contribute positively to the growth of $\mathbb{R}_0$, especially at higher τ. This confirms that b_u and a_p play a significant role in enhancing the reproduction number as Δ approaches unity.

In contrast, Figure 3.5 displays the effect of a_p and Δ_p, where increasing a_p leads to a rise in $\mathbb{R}_0$, while increasing Δ_p suppresses it. Once again, larger fractional orders amplify these effects. Among the parameters analyzed, b_u and a_p consistently exhibit the strongest influence on increasing $\mathbb{R}_0$, making them critical targets for intervention. Conversely, Δ_p demonstrates a significant inverse impact, effectively reducing $\mathbb{R}_0$ when increased.

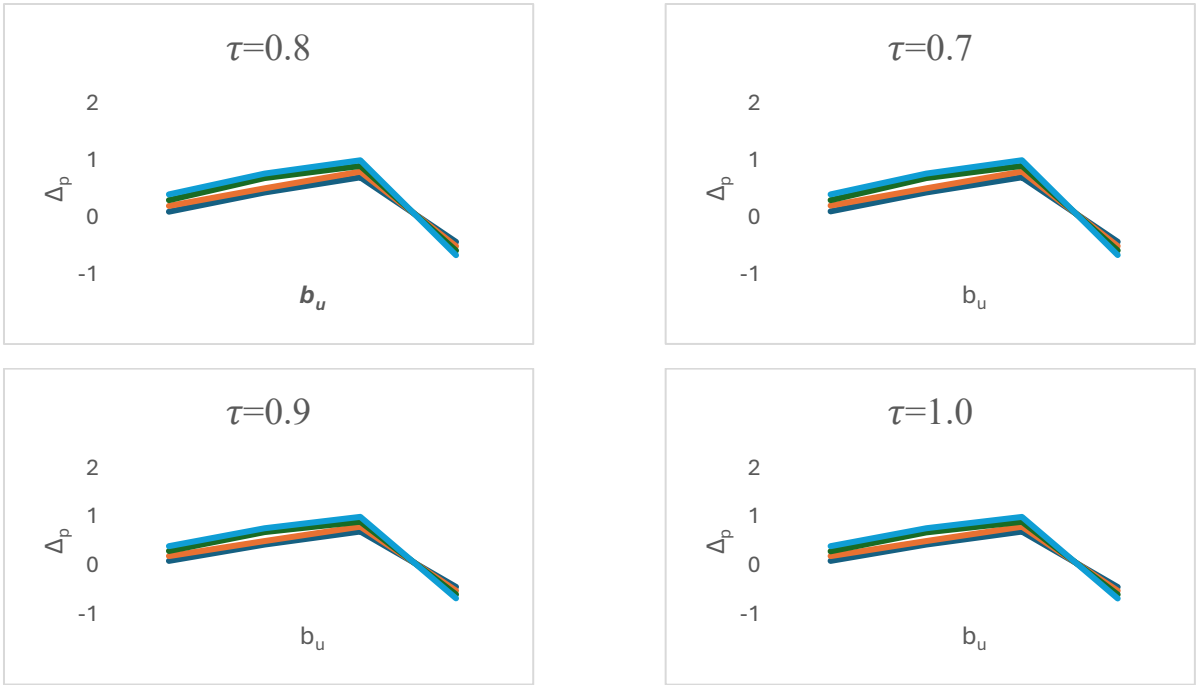

Fig. 2: Contour Plots of $\mathbb{R}_\psi$ as A Function of Parameters B_U and Δ_P for Various Values Of T.

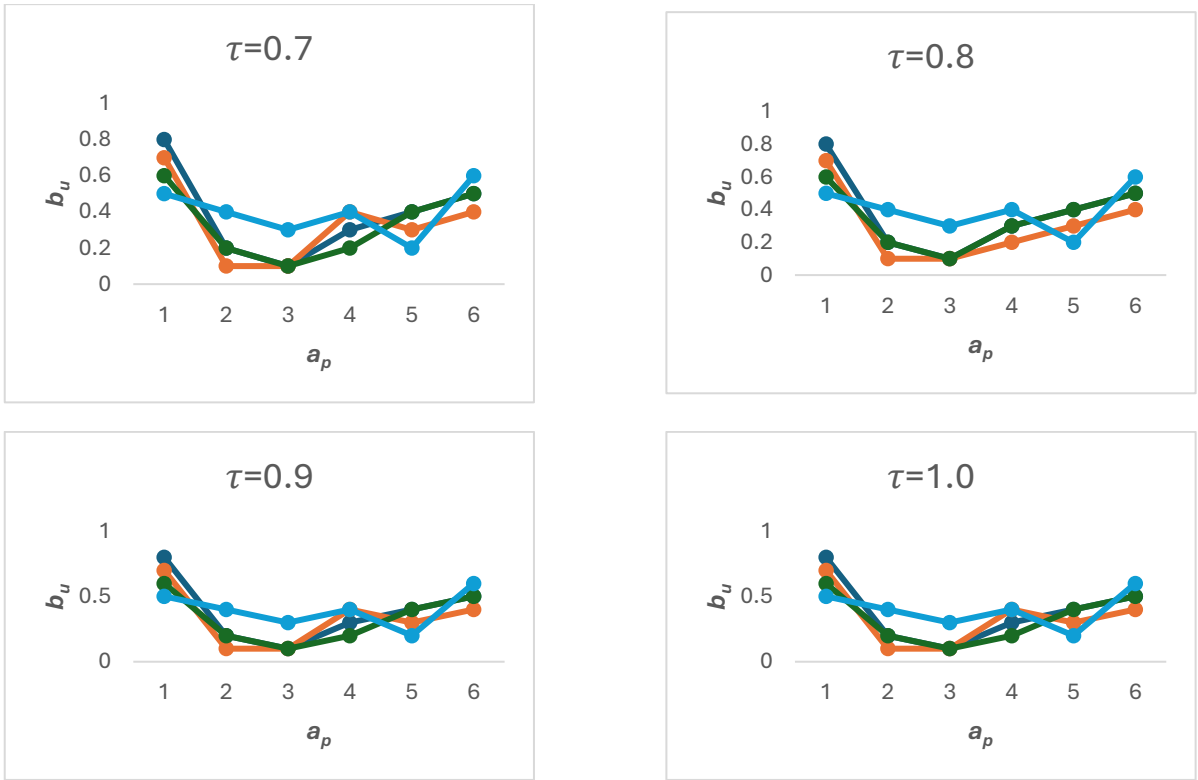

Fig. 3: Contour Plots of $\mathbb{R}_\psi$ as A Function of Parameters A_P and B_U for Various Values of T.

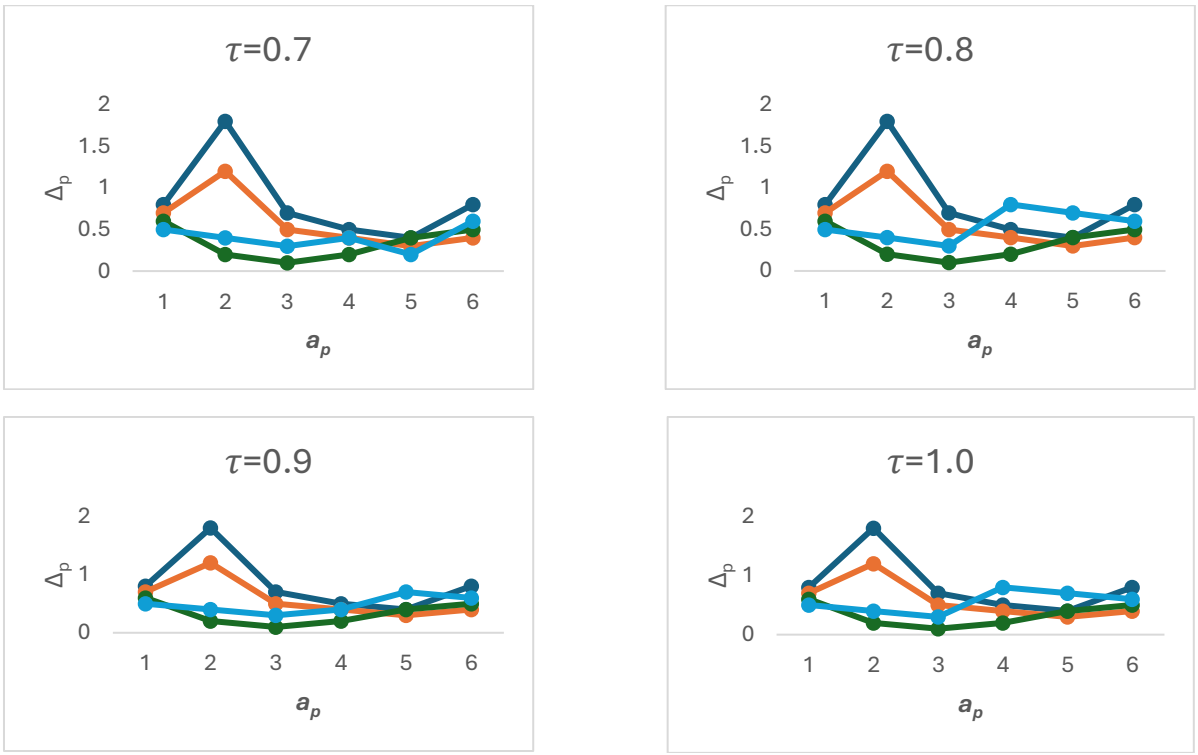

Fig. 4: Contour Plots of $\mathbb{R}_{\psi}$ as A Function of Parameters A_P and Δ_P for Various Values of T.

Figure 3.5 shows the surface plots of $\mathbb{R}_0$ as a function of the parameters b_u, a_p, and Δ_p. Subfigure 3.5 (a) presents $\mathbb{R}_0$ as a function of b_u and a_p, Subfigure 3.5 (b) shows $\mathbb{R}_0$ as a function of b_u and Δ_p, and Subfigure 3.5 (c) displays $\mathbb{R}_0$ as a function of a_p and Δ_p, all with varying fractional orders.

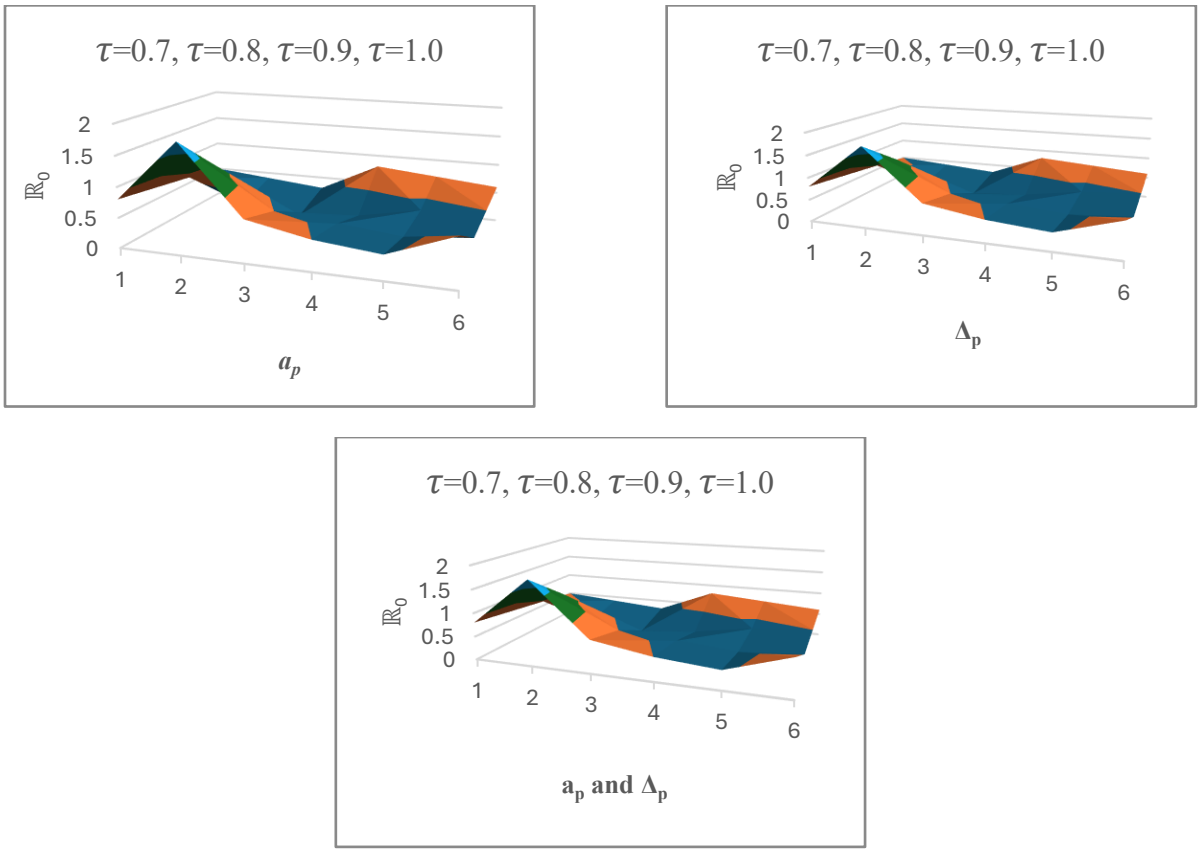

Fig. 5: 3D Surface Plots of $\mathbb{R}_{\psi}$ with Respect to B_U, A_P, and Δ_P. Different Curves Correspond to Varying Values of Δ.

The plots in Figure 3.5 illustrate the behavior of $\mathbb{R}_0$ with respect to the parameters b_u, a_p, and Δ_p under different fractional orders τ. In subfigure (3.5a), $\mathbb{R}_0$ increases nonlinearly with b_u, and the magnitude of $\mathbb{R}_0$ is higher for larger values of τ, indicating that the reproduction number becomes more sensitive to b_u as the fractional order increases. Subfigure (3.5b) shows a nearly linear relationship between $\mathbb{R}_0$ and a_p, with steeper slopes observed for higher τ, suggesting a stronger impact of virus production at elevated fractional orders.

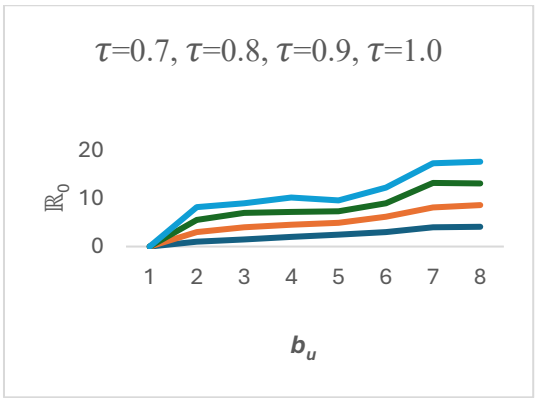

(A) $\mathbb{R}_0$ Vs b_u, For $a_p = 2, \Delta_p = 0.2$.

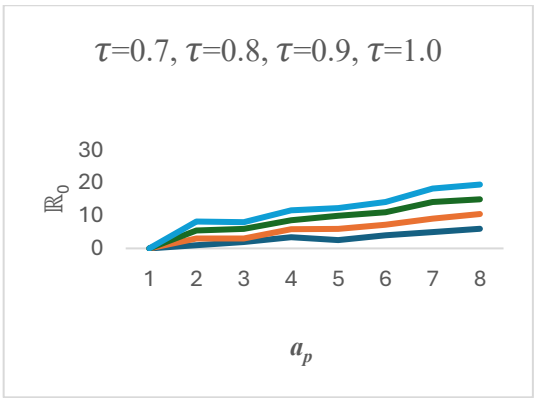

(B) $\mathbb{R}_0$ Vs a_p, For $b_u = 0.1, \Delta_p = 0.2$.

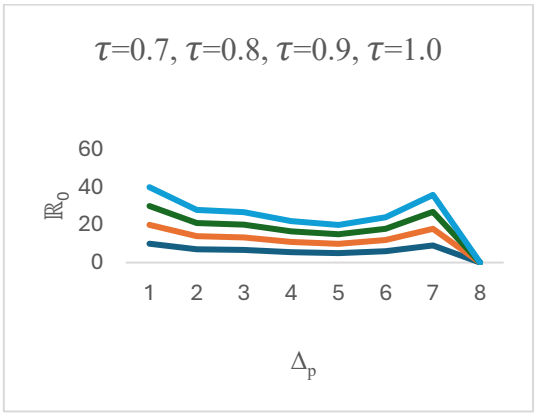

(C) $\mathbb{R}_0$ Vs Δ_p, For $b_p = 0.1, a_p = 2$.

Fig. 6: Variation of $\mathbb{R}_\psi$ with B_U, A_V, and Δ_P Across Fractional Orders, Highlighting Steeper Trends at Higher T.

In subfigure (3.5c), $\mathbb{R}_0$ decreases with increasing Δ_p, and the rate of decrease is more pronounced for larger τ, highlighting the enhanced suppressive effect of viral clearance at higher memory levels. These observations confirm that the fractional order τ modulates the system's memory and significantly influences the sensitivity of $\mathbb{R}_0$ to key biological parameters.

4. Numerical Simulations, Stability Analysis, and ANN-Based Approximation

This section covers the numerical stability analysis, examines population responses to NK cell activation, and implements ANN-based approaches to approximate system dynamics and $\mathbb{R}_0$.

The neural network architecture consists of a feedforward structure with a single input neuron, one hidden layer with 60 neurons, and an output layer comprising 16 neurons, each corresponding to a model state under various fractional orders. Each layer applies a linear transformation followed by a nonlinear activation, allowing the network to learn complex input–output relationships. The hidden layer utilizes the hyperbolic tangent sigmoid activation function, whereas the output layer adopts a linear activation to generate continuous-valued predictions. Training was performed in MATLAB R2023b using the Levenberg–Marquardt optimization algorithm. The dataset was randomly partitioned using the divider and function into training (70%), validation (15%), and testing (15%) subsets. The training settings included a maximum of 500 epochs, a minimum gradient tolerance of 10^{-15}, and a validation failure limit of 50 to promote stable convergence and reduce overfitting. Mean squared error (MSE) served as the performance criterion during both training and evaluation.

The populations u, v, p, and q evolve through nonlinear interactions determined by rescaled parameters derived from underlying biological rates and threshold values.

4.1. Numerical investigation and stability analysis of equilibrium points

The nondimensionalized model presented in Equation 10 forms the foundation for the numerical investigations. To compute the numerical solutions, the method described in equation (7) is employed. This scheme results from applying the transformation $s + \tau = m$ to system (11) and is implemented using MATLAB R2023b. For simulations, parameter values reported in [25] are adopted and listed in Table 2. Notably, the populations, cancer cells (u), infected cancer cells (v), free virus particles (p), and NK cells (q), are treated as relative, while time is considered discrete and relative, governed by the discrete fractional difference equations.

$$\begin{cases} u(t) = u(0) + \frac{1}{\Gamma(\tau)}\sum_{m=1}^{n} \frac{\Gamma(n-m+\tau)}{\Gamma(n-m+1)}\left(k_1^{\tau}u(m-1)\left(1-u(m-1)\right) - b_u^{\tau}u(m-1)p(m-1) - c_1^{\tau}x(m-1)q(m-1)\right), \\ v(t) = v(0) + \frac{1}{\Gamma(\tau)}\sum_{m=1}^{n} \frac{\Gamma(n-m+\tau)}{\Gamma(n-m+1)}\left(b_u^{\tau}u(m-1)p(m-1) - c_2^{\tau}v(m-1)q(m-1) - v(m-1)\right), \\ p(t) = p(0) + \frac{1}{\Gamma(\tau)}\sum_{m=1}^{n} \frac{\Gamma(n-m+\sigma)}{\Gamma(n-m+1)}\left(a_p^{\tau}v(m-1) - b_u^{\tau}u(m-1)p(m-1) - \Delta_p^{\tau}p(m-1)\right), \\ q(t) = q(0) + \frac{1}{\Gamma(\tau)}\sum_{m=1}^{n} \frac{\Gamma(n-m+\sigma)}{\Gamma(n-m+1)}\left(k_2^{\tau}v(m-1)q(m-1) - \Delta_q^{\tau}q(m-1)\right). \end{cases} \quad (17)$$

To increase the value of n_{max} in the solution (7), the following identity can be used, which enables extending n_{max} from a few hundreds to several thousand [13]:

$$\frac{\Gamma(n-m+\tau)}{\Gamma(n-m+1)} = e^{\ln\Gamma(n-m+\tau)-\ln\Gamma(n-m+1)}.$$

This modification facilitates efficient computation for large n_{max} values. Additionally, the nondimensionalization is performed by normalizing all population variables with respect to the cancer cell carrying capacity and rescaling time using the death rate of infected cancer cells. As a result of this transformation, the parameter values in system 4 are specified as $\Delta_q = 0.036, \Delta_p = 0.2, k_2 = 0.6, c_2 = 0.48, c_1 = 0.36, a_u = 0.1$, and $k_1 = 0.36$, as detailed in Table 2.

Table 2: List of the Parameters in This Study [25]

Parameters	Value	Units
Ξ	2.0×10^{-2}	$\frac{1}{h}$
ϖ_1	$\frac{7}{10} \times 10^{-9}$	$\frac{mm^3}{h}$ virus
χ	2.9×10^{-7}	$\frac{mm^3}{h}$ NK cell
ψ	2.9×10^{-6}	$\frac{mm^3}{h}$ NK cell
Δ_1	$\frac{1}{18}$	$\frac{1}{h}$
a_p	Variable	Virus – cell
Δ_2	0.0118	$\frac{1}{h}$
Ξ_q	5.6×10^{-7}	$\frac{1}{h}$ infected cancer cell
Δ_3	4.1×10^{-3}	$\frac{1}{h}$

We began by setting the bursting size of the virus to $b_v = 2$ and the NK cell (z) stimulation rate to $r_2 = 0.3$. These values satisfy the condition $b_u^\tau < \frac{\Delta_p^\tau}{a_p^\tau - 1}$, which ensures that $E_1(1,0,0,0)$ is locally asymptotically for all considered fractional orders $\tau = 0.7, 0.8, 0.9, 1$, as shown in Table 3.

Figures 7 and 8 illustrate the time evolution of the system components, under two different sets of initial conditions. In each case, the cancer cell population u(n) grows and stabilizes at its maximum value (carrying capacity), while all other populations $(v(n), p(n), q(n))$ decay to zero. This outcome represents treatment failure: the immune and viral forces are too weak to suppress tumor growth.

Table 3: Verification of the Inequality $B_U^T < \frac{\Delta_P^T}{A_P^T - 1}$ for Different Values of T

τ	b_u^τ	$\frac{\Delta_p^\tau}{a_p^\tau - 1}$	$b_u^\tau < \frac{\Delta_p^\tau}{a_p^\tau - 1}$
0.7	0.199526	0.519021	✓
0.8	0.158489	0.372346	✓
0.9	0.125893	0.271254	✓
1.0	0.100000	0.200000	✓

Importantly, the effect of the fractional order τ is visible in how fast the system reaches equilibrium. Lower values of τ lead to slower convergence due to memory effects inherent in fractional-order systems. These effects allow the system to retain past information, resulting in delayed responses. In contrast, the classical case $\tau = 1$ shows the fastest stabilization.

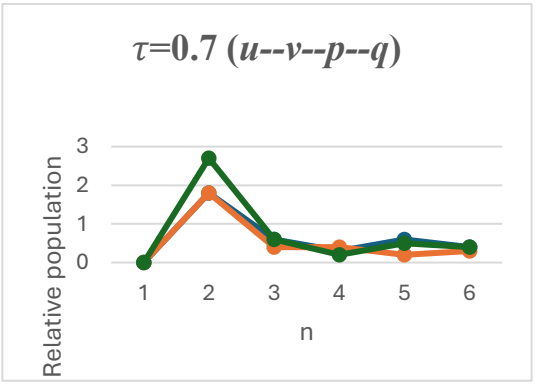

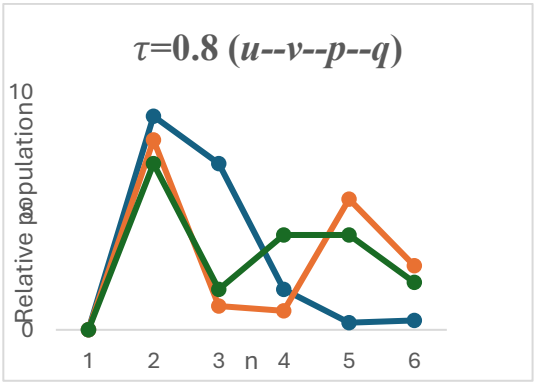

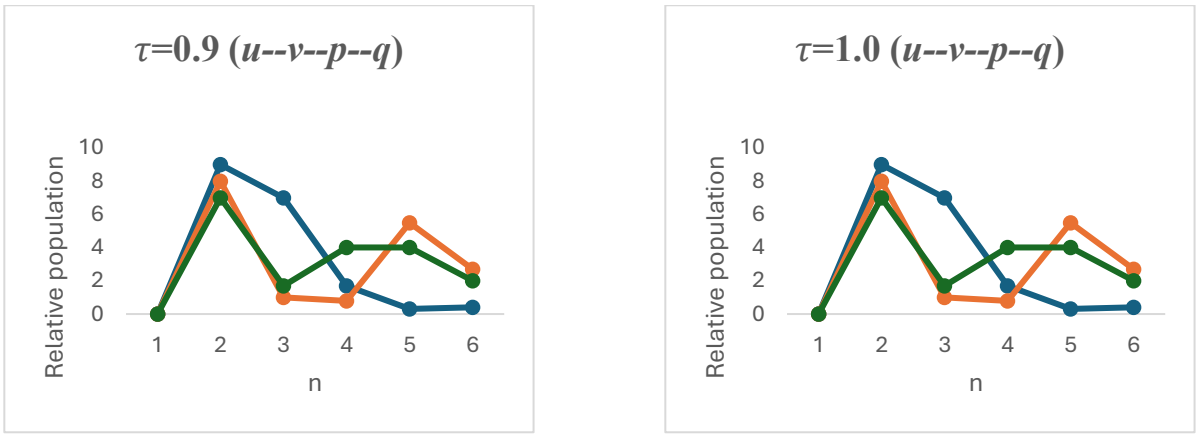

Fig. 7: Population Dynamics of U, V, P, and Q Over Time for Various Values of T, with $U(0) = 0.5, V(0) = 0, P(0) = 0.3, Q(0) = 0.1$, where $A_P = 2, K_2 = 0.3$.

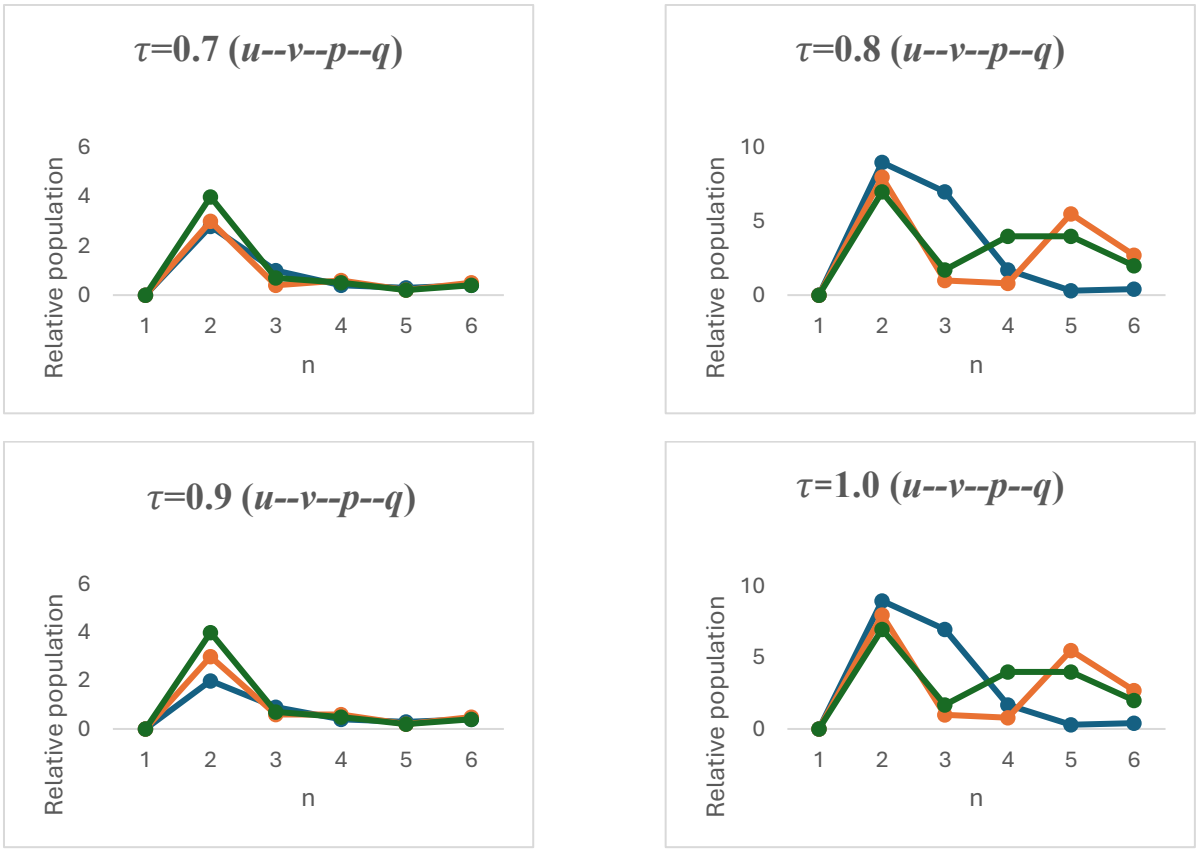

Fig. 8: Population Dynamics of U, V, P, and Q Over Time for Various Values of T, with $U(0) = 0.9, V(0) = 0, P(0) = 0.7, Q(0) = 0.2$, where $A_P = 2, K_2 = 0.3$.

Interestingly, a transient dip in the cancer population $u(n)$ is observed in Figure 4.1 for $\tau = 1$ before its rapid rise toward equilibrium, whereas this dip is less apparent for lower fractional orders. Despite these temporal variations, all trajectories ultimately converge to the same steady state, confirming the theoretical prediction of E_1 's stability across the fractional orders.

Next, we increased the viral bursting size to $b_v = 5$ while keeping $r_2 = 0.3$ unchanged. Under this configuration, the system satisfies the stability conditions $b_u^\tau < \frac{\Delta_p^\tau (a_p^\tau + 1)}{a_p^\tau - 1} + 1$ and $v_2 < \frac{\Delta_u^\tau}{k_2^\tau}$, which ensure that the equilibrium point $E_2(u_2, v_2, p_2, 0)$ becomes locally asymptotically stable for all $\tau = 0.7, 0.8, 0.9, 1$, as shown in Table 4.

Table 4: Verification of the Inequalities $B_U^T < \frac{\Delta_P^T (A_P^T + 1)}{A_P^T - 1} + 1$ and $V_2 < \frac{\Delta_Q^T}{K_2^T}$ for Different Values of T

τ	b_u^τ	$\frac{\Delta_p^\tau (a_p^\tau + 1)}{a_p^\tau - 1} + 1$	$b_u^\tau < \frac{\Delta_p^\tau (a_p^\tau + 1)}{a_p^\tau - 1} + 1$	v_2	$\frac{\Delta_u^\tau}{k_2^\tau}$	$v_2 < \frac{\Delta_u^\tau}{k_2^\tau}$
0.7	0.199526	1.635020	✓	0.090000	0.226687	✓
0.8	0.158489	1.486280	✓	0.090000	0.183377	✓
0.9	0.125893	1.379190	✓	0.090000	0.148342	✓
1.0	0.100000	1.300000	✓	0.090000	0.120000	✓

Figures 9 and 10 show that the cancer cell (u) population stabilizes at a value less than 1, while infected cancer cells and viruses approach positive steady states. The NK cell (q) population gradually disappears, indicating that the virus alone is sufficient to keep the tumor

under control. The memory effect again slows the transition for smaller τ values, but all trajectories converge to the same equilibrium, confirming the stability of E_2 under the given conditions.

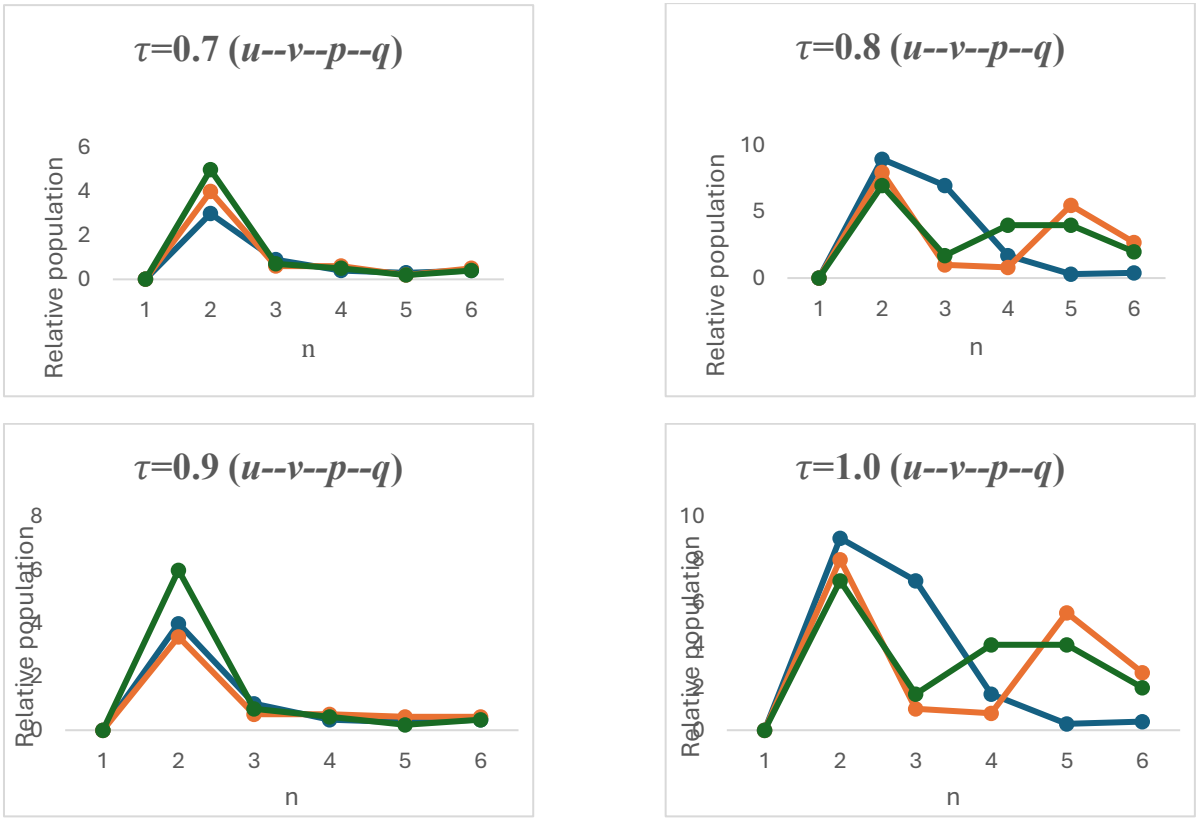

Fig. 9: Population Dynamics of U, V, P, and T Over Time for Various Values of T, with $U(0) = 0.5, V(0) = 0, P(0) = 0.3, Q(0) = 0.1$, where $A_P = 5, K_2 = 0.3$.

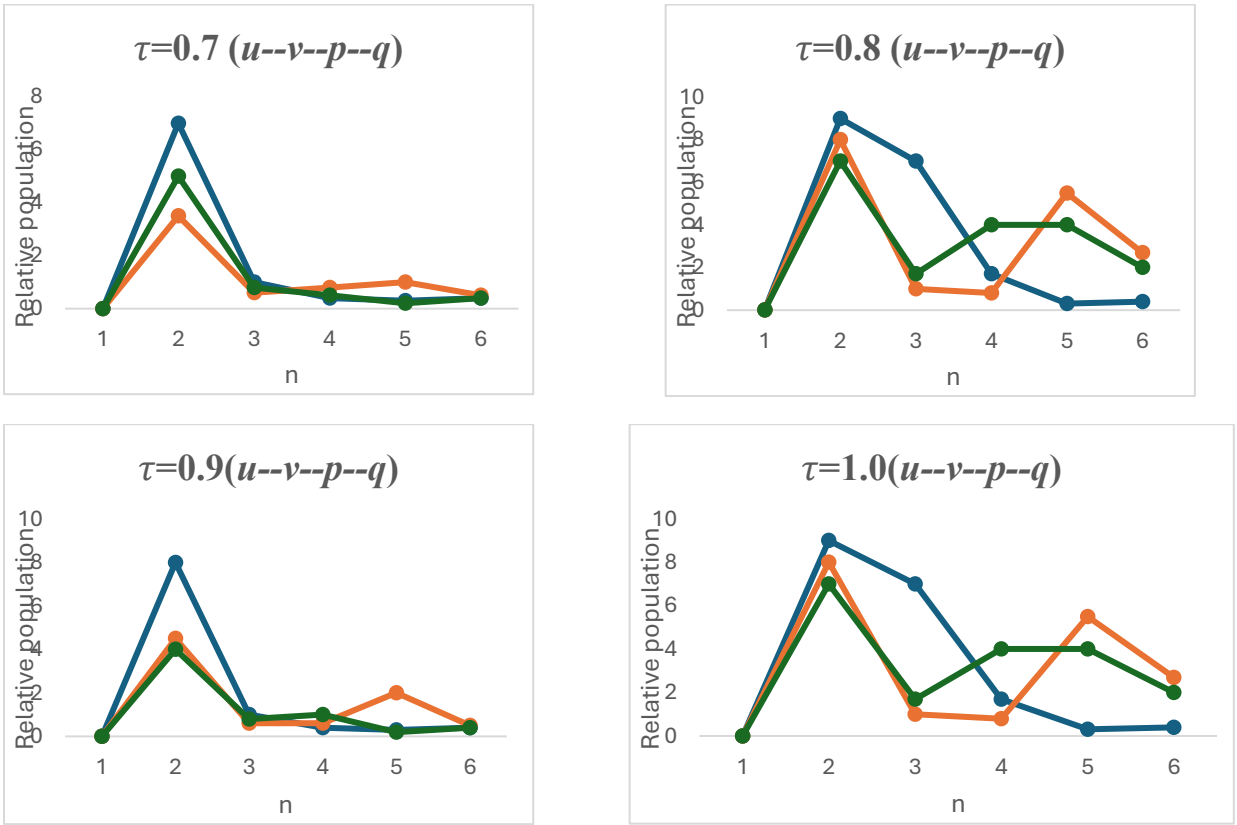

Fig. 10: Population Dynamics of U, V, P, and Q Over Time for Various Values of T, with $U(0) = 0.9, V(0) = 0, P(0) = 0.7, Q(0) = 0.2$, where $A_P = 5, K_2 = 0.3$.

The fractional-order parameter σ influences not only the transient dynamics but also the location of the equilibrium point. While all trajectories converge to steady states for different σ, the exact values of the equilibrium components vary with σ. This behavior highlights the sensitivity of the system to memory effects, yet confirms the local stability of E_2 under each configuration.

Finally, the viral bursting size and NK stimulation rate were increased to $a_q = 5$ and $k_2 = 0.7$, respectively. In this setting, the system satisfies the conditions $b_1 > 0, b_2 > 0, b_3 > 0, b_4 > 0$, and $b_1 b_2 b_3 > b_3^2 + b_1^2 b_4$, which guarantee the local asymptotic stability of the full coexistence equilibrium $E_3(u_+^*, v^*, p_-^*, q_+^*)$. This holds for all values of $\tau = 0.8, 0.9, 1$, while one condition is violated at $\tau = 0.7$, as $b_4 < 0$.

Table 5 presents the numerically computed equilibrium values u_+^*, v^*, p_-^*, and q_+^* at different fractional orders τ, showing how the steady-state solutions vary with memory effects. The value of q_3 becomes negative at $\tau = 0.7$, which is biologically infeasible and indicates instability of the equilibrium in this case.

Table 5: Equilibrium Values T, U_+^*, V^*, P_-^* and Q_+^* at Different Fractional Orders T

τ	u_+^*	v^*	p_-^*	q_+^*
0.7	0.732982	0.125269	0.821623	-0.068149
0.8	0.670182	0.093103	0.882859	0.012972
0.9	0.609240	0.069196	0.945210	0.092321
1.0	0.551586	0.051429	1.007777	0.168476

To rigorously verify the stability, Table 6 lists the computed RH coefficients b_1, b_2, b_3, b_4 and checks each stability condition individually. The final column confirms whether the compound inequality $b_1 b_2 b_3 > b_3^2 + b_1^2 b_4$ is satisfied. As observed, all conditions are met for $\tau \geq 0.784$, supporting the conclusion that E_3 is locally asymptotically stable in this range. As before, lower values of τ lead to slower convergence, but the final state is unchanged. This confirms that E_3 remains stable across all tested fractional orders and reflects a scenario where the immune response, aided by a high viral load, keeps the tumor in check.

As shown in Figures 11 and 12, all four populations settle at positive values for $\tau = 0.8, 0.9, 1$, indicating that the cancer, infected, viruses, and NK cells coexist in a stable dynamic balance. This confirms the local asymptotic stability of the full coexistence equilibrium E_3 within this range. Although the simulation at $\tau = 0.7$ exhibits similar dynamic behavior, the RH condition $b_4 > 0$ is violated, suggesting potential instability from.

Table 6: Verification of RH Conditions for Stability of E_3 at Different Values of T

τ	b_1	b_2	b_3	b_4	$b_1 > 0$	$b_2 > 0$	$b_3 > 0$	$b_4 > 0$	$b_1 b_2 b_3 > b_3^2 + b_1^2 b_4$
0.7	1.78812	0.48458	0.04455	-0.00158	✓	✓	✓	×	✓
0.8	1.68533	0.39684	0.03963	0.00016	✓	✓	✓	✓	✓
0.9	1.60223	0.32346	0.03255	0.00061	✓	✓	✓	✓	✓
1.0	1.53460	0.26264	0.02546	0.00060	✓	✓	✓	✓	✓

a theoretical perspective. Moreover, the steady-state levels of each population vary with τ, reflecting the impact of memory effects on long-term dynamics. Lower τ values lead to slower convergence and slightly altered equilibrium values, while higher τ values yield faster transitions and more pronounced transients. The coexistence of all four populations and the instability of the other equilibria (E_1 and E_2) demonstrate that E_3 is the only stable equilibrium in the biologically relevant domain D for $\tau \geq 0.784$.

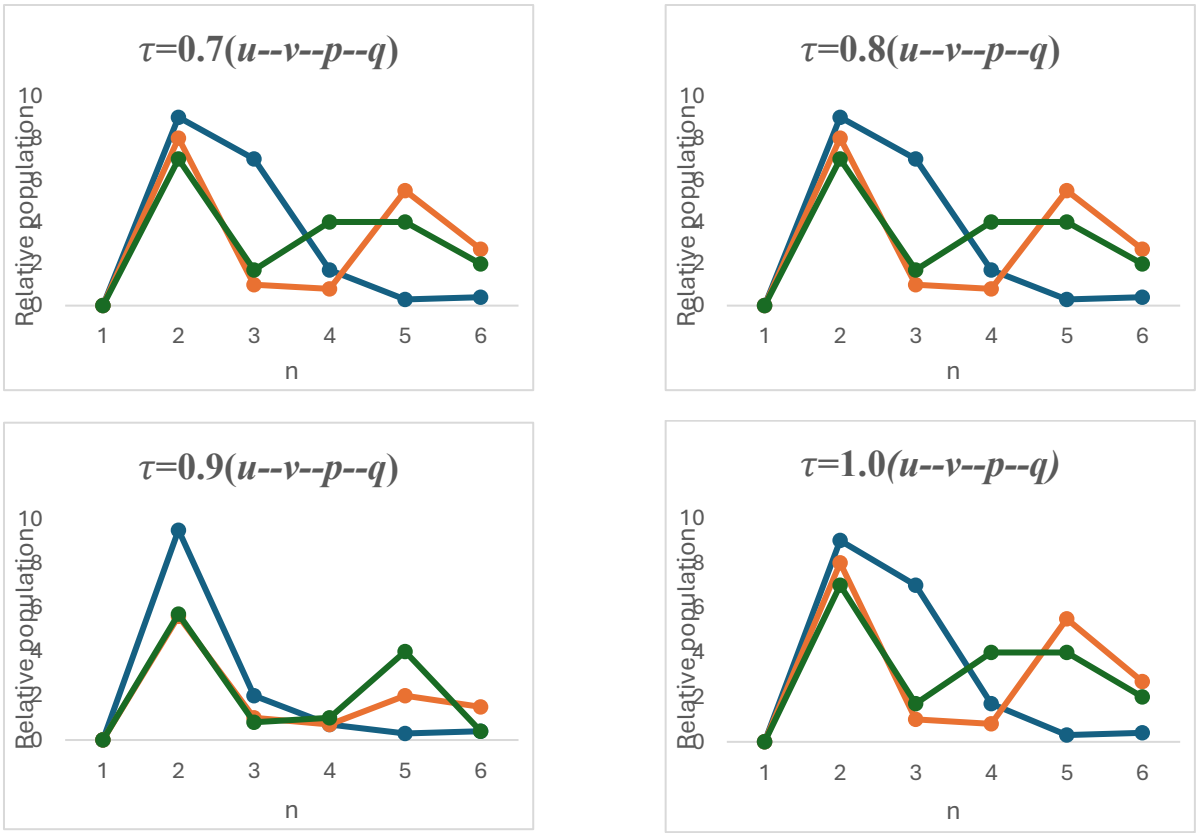

Fig. 11: Population Dynamics of X, Y, V, and Z Over Time for Various Values of Σ, with $X(0) = 0.5, Y(0) = 0, V(0) = 0.3, Z(0) = 0.1$, where $B_N = 5, R_2 = 0.7$.

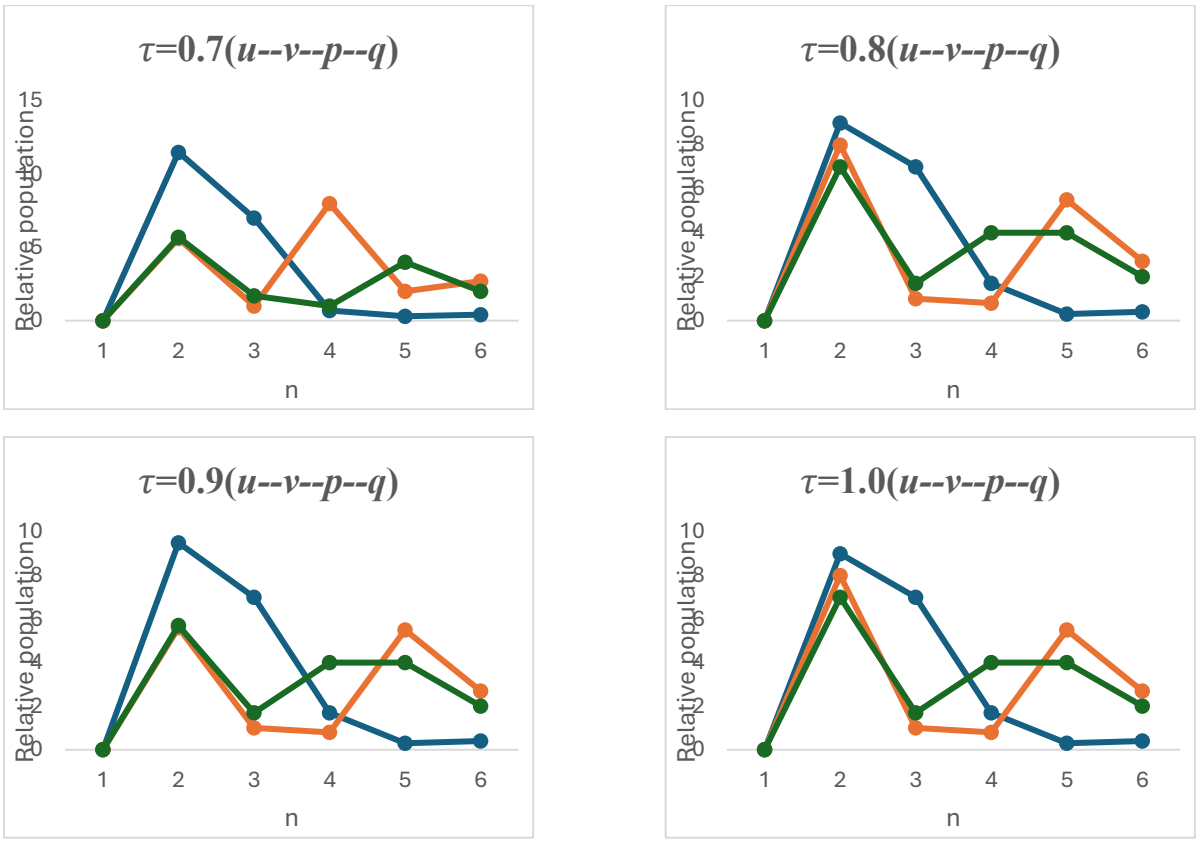

Fig. 12: Population Dynamics of $U, V, P,$ and Q Over Time for Various Values of T, with $U(0) = 0.9, V(0) = 0, P(0) = 0.7, Q(0) = 0.2$, where $A_P = 5, K_2 = 0.7$.

5. Conclusion

This study developed a discrete fractional-order model to analyze interactions among cancer cells, oncolytic viruses, and NK cells during oncolytic virotherapy (OV). By incorporating the fractional-order parameter σ,the model captured memory-dependent dynamics for more realistic biological representation. Existence and local stability of equilibria were established using fixed-point theorems, next-generation matrix methods, and discrete RH criteria. Sensitivity analysis showed that the viral burst size ($\mathbb{R}_0$) was evaluated in response to key parameters (b_u, a_p, and Δ_p) and fractional orders. The results demonstrated that the viral burst size (a_p) and the rescaled infection parameter ($b_u = \frac{\varpi_1 C}{\Delta_1}$) have a strong positive influence on $\mathbb{R}_0$, while the rescaled viral clearance rate ($\Delta_p = \frac{\Delta_2}{\Delta_1}$) exerts a suppressive effect. Notably, these sensitivities intensified as the fractional order σ approached unity, highlighting the impact of memory effects on therapeutic dynamics. Simulation results revealed three major therapeutic regimes corresponding to different combinations of a_p and k_2: (1) complete treatment failure with tumor dominance, (2) partial control where viruses suppress tumors without immune involvement, and (3) full coexistence where both viruses and NK cells cooperate to restrain tumor growth. The coexistence equilibrium (E_3) was shown to be locally asymptotically stable for $\tau \geq 0.784$, whereas lower values led to instability or biologically infeasible solutions, confirming the critical role of immune activation thresholds and memory effects. To further enhance computational efficiency, a feedforward ANN was trained to approximate both the system dynamics and the basic reproduction number. The ANN achieved outstanding performance across all tested conditions, with high regression coefficients ($R \geq 0.998$) and low absolute errors. This surrogate model accurately reproduced the time evolution of each population and offered real-time prediction capabilities, enabling fast exploration of parameter spaces and treatment scenarios. Overall, integrating fractional modeling with neural networks proved effective for simulating and optimizing cancer-virus-immune interactions, supporting the design of improved virotherapy strategies.

Future Directions

Future research may further explore the integration of fractional-order modeling with neural network–based learning to enhance the simulation, prediction, and optimization of complex cancer–immune–virus dynamics. Such a framework has the potential to support the development of more effective virotherapy protocols by identifying optimal parameter combinations and treatment strategies, particularly in the presence of biological uncertainty and patient-level variability.

Declaration

Conflicts of Interest: Authors declare that there is no conflict of interest with this paper.

References

[1] O. W. Abdulwahhab and N. H. Abbas. A new method to tune a fractional-order pid controller for a twin rotor aerodynamic system. Arabian Journal for Science and Engineering, 42:5179-5189, 2017. https://doi.org/10.1007/s13369-017-2629-5

[2] A. Al-Khedhairi, A. A. Elsadany, and A. Elsonbaty. On the dynamics of a discrete fractional-order cournot-bertrand competition duopoly game. Mathematical Problems in Engineering, page Article ID 8249215, 2022. https://doi.org/10.1155/2022/8249215.

[3] S. M. Al-Tuwairqi, N. O. Al-Johani, and E. A. Simbawa. Modeling dynamics of cancer virotherapy with immune response. Advances in Difference Equations, 2020:438, 2020.

[4] Z. Ali. Theoretical and Computational Study of Fractional-order Mathematical Models for Infectious Diseases. PhD thesis, Monash University, 2023.

[5] Z. Ali, S. N. Nia, F. Rabiei, K. Shah, and M. K. Tan. A semi-analytical approach for the solution of time-fractional navier-stokes equation. Advances in Mathematical Physics, page Article ID 5547804, 2021. 13 pages. https://doi.org/10.1155/2021/5547804.

[6] Z. Ali, F. Rabiei, K. Shah, and Z. A. Majid. Dynamics of sir mathematical model for covid-19 outbreak in pakistan under fractal-fractional derivative. Fractals, 29(5):2150120, 2021. https://doi.org/10.1142/S0218348X21501206.

[7] A. M. Alqahtani, S. Akram, J. Ahmad, K. A. Aldwoah, and M. ur Rahman. Stochastic wave solutions of fractional radhakrishnan-kundu-lakshmanan equation arising in optical fibers with their sensitivity analysis. Journal of Optics, 2024. https://doi.org/10.1007/s12596-024-01850-w.

[8] J. Altomonte, L. Wu, M. Meseck, L. Chen, O. Ebert, A. Garcia-Sastre, J. Fallon, J. Mandeli, and S. L. Woo. Enhanced oncolytic potency of vesicular stomatitis virus through vector-mediated inhibition of nk and nkt cells. Cancer Gene Therapy, 16:266-278, 2009. https://doi.org/10.1038/cgt.2008.74.

[9] C. A. Alvarez-Breckenridge et al. Nk cells impede glioblastoma virotherapy through nkp30 and nkp46 natural cytotoxicity receptors. Nature Medicine, 18:1827-1834, 2012. https://doi.org/10.1038/nm.3013

[10] S. C-Vázquez et al. Applications of fractional operators in robotics: A review. Journal of Intelligent and Robotic Systems, 104:63, 2022. https://doi.org/10.1007/s10846-022-01597-1.

[11] N. H. Can, H. Jafari, and M. N. Ncube. Fractional calculus in data fitting. Alexandria Engineering Journal, 59(5):3269-3274, 2020. https://doi.org/10.1016/j.aej.2020.09.002.

[12] C. Coll, A. Herrero, D. Ginestar, and E. Sánchez. The discrete fractional order difference applied to an epidemicmodel with indirect transmission. Applied Mathematical Modelling, 103:636-648, 2022. https://doi.org/10.1007/s10846-022-01597-1.

[13] M. F. Danca. Fractional order logistic map: Numerical approach. Chaos, Solitons and Fractals, 157:111851, 2022. https://doi.org/10.1016/j.chaos.2022.111851.

[14] S. Das. Application of generalized fractional calculus in electrical circuit analysis and electromagnetics. In Functional Fractional Calculus. Springer, Berlin, Heidelberg, 2011. https://doi.org/10.1007/978-3-642-20545-3_8.

[15] E. C. de Oliveira and J. A. T. Machado. A review of definitions for fractional derivatives and integral. Mathematical Problems in Engineering, 2014:238459, 2014. 6 pages. https://doi.org/10.1155/2014/238459.

[16] A. Desjardins et al. Recurrent glioblastoma treated with recombinant poliovirus. New England Journal of Medicine, 379:150-161, 2018. https://doi.org/10.1056/NEJMoa1716435

[17] N. Djenina, A. Ouannas, I. M. Batiha, G. Grassi, T.-E. Oussaeif, and S. Momani. A novel fractional-order discrete sir model for predicting covid-19 behavior. Mathematics, 10(13):2224, 2022. https://doi.org/10.3390/math10132224

[18] A. Elsonbaty and A. A. Elsadany. On discrete fractional-order lotka-volterra model based on the caputo difference discrete operator. Mathematical Sciences, 17(1):67-79, 2023. https://doi.org/10.1007/s40096-021-00442-0

[19] P. F. Ferrucci, L. Pala, F. Conforti, and E. Cocorocchio. Talimogene laherparepvec (t-vec): An intralesional cancer immunotherapy for advanced melanoma. Cancers, 13:1383, 2021. https://doi.org/10.3390/cancers13061383.

[20] B. Gesundheit et al. Effective treatment of glioblastoma multiforme with oncolytic virotherapy: A case-series. Frontiers in Oncology, 10:702, 2020. https://doi.org/10.3389/fonc.2020.00702

[21] J. Han, C. A. Alvarez-Breckenridge, Q. E. Wang, and J. Yu. Tgf-beta signaling and its targeting for glioma treatment. American Journal of Cancer Research, 5:945-955, 2015.

[22] R. Hilfer. Applications of Fractional Calculus in Physics. World Scientific, Singapore, 2000. https://doi.org/10.1142/3779.

[23] L.-L. Huang, J. H. Park, G.-C. Wu, and Z.-W. Mo. Variable-order fractional discrete-time recurrent neural networks. Journal of Computational and Applied Mathematics, 370:112633, 2020. https://doi.org/10.1016/j.cam.2019.112633.

[24] Y. Jiang et al. Fractional-order autonomous circuits with order larger than one. Journal of Advanced Research, 25:217-225, 2020. https://doi.org/10.1016/j.jare.2020.05.005.

[25] D. Kim, D.-H. Shin, and C. K. Sung. The optimal balance between oncolytic viruses and natural killer cells: A mathematical approach. Mathematics, 10:3370, 2022. https://doi.org/10.3390/math10183370.

[26] Y. Kim, J. Y. Yoo, T. J. Lee, J. Liu, J. Yu, M. A. Caligiuri, B. Kaur, and A. Friedman. Complex role of nk cells in regulation of oncolytic virus-bortezomib therapy. Proceedings of the National Academy of Sciences of the USA, 115:4927-4932, 2018. https://doi.org/10.1073/pnas.1715295115

[27] E. Y. L. Leung et al. Nk cells augment oncolytic adenovirus cytotoxicity in ovarian cancer. Molecular Therapy Oncolytics, 16:289-301, 2020. https://doi.org/10.1016/j.omto.2020.02.001.

[28] X. Li, P. Wang, H. Li, X. Du, M. Liu, Q. Huang, Y. Wang, and S. Wang. The efficacy of oncolytic adenovirus is mediated by t -cell responses against virus and tumor in syrian hamster model. Clinical Cancer Research, 23:239-249, 2017. https://doi.org/10.1158/1078-0432.CCR-16-0477

[29] Y. A. Madani, Z. Ali, M. Rabih, A. Alsulami, N. H. E. Eljaneid, K. Aldwoah, and B. Muflh. Discrete fractional-order modeling of recurrent childhood diseases using the caputo difference operator. Fractal and Fractional, 9(1):55, 2025. https://doi.org/10.3390/fractalfract9010055

[30] Y. A. Madani, M. N. A. Rabih, F. A. Alqarni, Z. Ali, K. A. Aldwoah, and M. Hleili. Existence, uniqueness, and stability of a nonlinear tripled fractional order differential system. Fractal and Fractional, 8(7):416, 2024. https://doi.org/10.3390/fractalfract8070416.

[31] R. L. Magin. Fractional calculus in bioengineering. Critical Reviews in Biomedical Engineering, 32(1):1-104, 2004. https://doi.org/10.1615/CritRevBiomedEng.v32.10.

[32] R. Matušu. Application of fractional order calculus to control theory. International Journal of Mathematical Models and Methods in Applied Sciences, 5(7):1162-1169, 2011.

[33] R. P. Meilanov and R. A. Magomedov. Thermodynamics in fractional calculus. Journal of Engineering Physics and Thermophysics, 87:1521-1531, 2014. https://doi.org/10.1007/s10891-014-1158-2.

[34] F. Meral, T. Royston, and R. Magin. Fractional calculus in viscoelasticity: an experimental study. Communications in Nonlinear Science and Numerical Simulation, 15:939-945, 2010. https://doi.org/10.1016/j.cnsns.2009.05.004.

[35] M. Mondal, J. Guo, P. He, and D. Zhou. Recent advances of oncolytic virus in cancer therapy. Human Vaccines [6] Immunotherapeutics, 16:2389-2402, 2020. https://doi.org/10.1080/21645515.2020.1723363.

[36] K. Oldham. Fractional differential equations in electrochemistry. Advances in Engineering Software, 41:9-12, 2010. https://doi.org/10.1016/j.advengsoft.2008.12.012

[37] P. Ostalczyk. Discrete Fractional Calculus: Applications in Control and Image Processing, volume 4. World Scientific, 2015. https://doi.org/10.1142/9833.

[38] Y. Peng, S. He, and K. Sun. Chaos in the discrete memristor-based system with fractional-order difference. Results in Physics, 24:104106, 2021. https://doi.org/10.1016/j.rinp.2021.104106

[39] T. A. Phan and J. P. Tian. The role of the innate immune system in oncolytic virotherapy. Computational and Mathematical Methods in Medicine, 2017:6587258, 2017. https://doi.org/10.1155/2017/6587258.

[40] N. S. Senekal, K. J. Mahasa, A. Eladdadi, L. de Pillis, and R. Ouifki. Natural killer cells recruitment in oncolytic virotherapy: A mathematical model. Bulletin of Mathematical Biology, 83:75, 2021. https://doi.org/10.1007/s11538-021-00903-6
[41] N. A. Shah, D. Vieru, and C. Fetecau. Effects of the fractional order and magnetic field on the blood flow in cylindrical domains. Journal of Magnetism and Magnetic Materials, 409:10-19, 2016. https://doi.org/10.1016/j.jmmm.2016.02.013.
[42] V. E. Tarasov. Fractional Dynamics: Applications of Fractional Calculus to Dynamics of Particles, Fields and Media. Springer Science and Business Media, 2011. https://doi.org/10.1007/978-3-642-14003-7
[43] V. E. Tarasov and V. V. Tarasova. Long and short memory in economics: fractional-order difference and differentiation. arXiv preprint arXiv:1612.07903, 2016. https://doi.org/10.21013/jmss.v5.n2.p10
[44] S. H. Thorne, T. H. Hwang, et al. Rational strain selection and engineering creates a broad-spectrum, systemically effective oncolytic poxvirus, jx-963. Journal of Clinical Investigation, 117:3350-3358, 2007. https://doi.org/10.1172/JCI32727.